

Rotations of large inertial cubes, cuboids, cones, and cylinders in turbulence

Nimish Pujara,^{1,*} Theresa B. Oehmke,¹ Ankur D. Bordoloi,² and Evan A. Variano¹

¹*Department of Civil and Environmental Engineering, University of California, Berkeley, California 94720, USA*

²*Physics Division, Los Alamos National Laboratory, Los Alamos, New Mexico 87545, USA*



(Received 8 March 2018; published 16 May 2018)

We conduct experiments to investigate the rotations of freely moving particles in a homogeneous isotropic turbulent flow. The particles are nearly neutrally buoyant and the particle size exceeds the Kolmogorov scale so that they are too large to be considered passive tracers. Particles of several different shapes are considered including those that break axisymmetry and fore-aft symmetry. We find that regardless of shape the mean-square particle angular velocity scales as $d_{eq}^{-4/3}$, where d_{eq} is the equivalent diameter of a volume-matched sphere. This scaling behavior is consistent with the notion that velocity differences across a length d_{eq} in the flow are responsible for particle rotation. We also find that the probability density functions (PDFs) of particle angular velocity collapse for particles of different shapes and similar d_{eq} . The significance of these results is that the rotations of an inertial, nonspherical particle are only functions of its volume and not its shape. The magnitude of particle angular velocity appears log-normally distributed and individual Cartesian components show long tails. With increasing d_{eq} , the tails of the PDF become less pronounced, meaning that extreme events of angular velocity become less common for larger particles.

DOI: [10.1103/PhysRevFluids.3.054605](https://doi.org/10.1103/PhysRevFluids.3.054605)

I. INTRODUCTION

Particles of different sizes and shapes are translated and rotated by the turbulent fluid motion in many examples of environmental flows, such as aerosols in the atmosphere or microplastics and plankton in the ocean. The particle motion matches that of the surrounding fluid for neutrally buoyant spheres that are small enough so that the fluid velocity varies linearly across the particle diameter. For particles that do not meet these constraints, additional considerations must be taken into account to understand their dynamics (see reviews [1–4]). In particular, it is difficult to create accurate models for particle motion where the size exceeds the Kolmogorov scale because the flow around the particle can no longer be assumed to be in the Stokes regime.

For spheres whose diameters are only small departures from the tracer limit, there exist models that can account for finite size effects (i.e., Faxén corrections [5–8] or modified Stokes numbers [9]). However, our focus is on particles that are large enough to be outside even these limits while remaining close to neutrally buoyant. The dynamics of such particles in turbulence are largely unknown, but they are likely to be functions of particle size and shape. The role of particle shape in determining a particle's angular velocity is particularly intriguing because nonspherical particles have multiple length scales which may allow particles to couple to turbulent motions in interesting ways.

Examples of coupling between particle shape and turbulence include rotations of large fibers in the slender body limit and rotations of small ellipsoids in the tracer limit, both of which have displayed

*pujara@berkeley.edu

interesting connections to turbulence theory. Laboratory measurements and simulations have shown that fibers in the slender body limit with lengths in the inertial subrange of turbulence have mean-square tumbling rates that show power law scaling with fiber length [10,11]. The scaling exponents can be predicted from Kolmogorov’s similarity hypotheses of moments of velocity increments across distances in the inertial subrange (henceforth K41 theory). In the tracer limit, the rotational kinematics of ellipsoids have been found to reveal features of the Lagrangian dynamics of the velocity gradient tensor [12–15]. Such ellipsoids follow fluid trajectories and rotate in response to the fluid rotation (vorticity) as well as the fluid strain rate due to their nonspherical shape [16]. However, it has been found that strain-rate contributions to mean-square rotation rate are canceled by vorticity-strain correlations along Lagrangian trajectories, leaving only vorticity contributions to the mean-square rotation rate [17]. Thus, the mean-square particle angular velocity is almost independent of the particle shape for ellipsoids in the tracer limit.

Previous laboratory work on the rotations of inertial spheres with diameter, d , much larger than the Kolmogorov scale, η , have shown that the magnitude of the particle angular velocity has PDFs that are fitted well by a log-normal model [18,19]. No clustering has been observed for these neutrally buoyant, $d \gg \eta$ particles [20], but there is evidence that lift forces may couple the rotational and translational motions [21]. Numerical simulations with access to the full velocity field in the immediate vicinity of large neutrally buoyant spheres have shown that turbulent statistics are modified locally for distances up to $2d$ around particles and that particles undergo some angular slip relative to the surrounding fluid [22].

The influence of particle shape on the rotation of inertial particles has been the subject of prior investigations by our research group [23–26]. These investigations have so far been unable to detect meaningful changes in the mean-square particle angular velocity due to effects of shape, but only axisymmetric shapes such as spheroids and cylinders have been tested and the effects of measurement noise on the results have not been fully understood. Herein we test the robustness of previous results by expanding the parameter space of particle shape to include conical particles and cuboid particles, which break fore-aft symmetry and axisymmetry, respectively. We also reanalyze data of cylindrical particles from Bordoloi and Variano [26] with a different method that is more robust to noise. Our goals are to understand the effects of particle shape and size on the mean-square particle angular velocity and the PDFs of particle angular velocity components.

The remainder of this paper is organised as follows. Section II describes the experimental setup and the methodology we use to compute particle angular velocity and quantify measurement noise. In Sec. III, we examine the shape and the moments of the particle angular velocity PDFs. We also compare our results to other studies to understand how particle size and shape influences rotational dynamics. We close with a summary of the main conclusions in Sec. IV.

II. METHODS

A. Laboratory experiments

We perform measurements of inertial particles advecting in the turbulent water tank shown schematically in Fig. 1 and described in detail in Ref. [27]. The tank is $80 \times 80 \times 360$ cm in the x , y , and z directions, respectively. Flow is generated by two randomly actuated synthetic jet arrays that face each other in which individual jets are driven stochastically to maximize turbulence intensity while minimizing the mean flow [28]. Two screens are installed at $z = \pm 37.5$ cm to separate inertial particles in the central region of the tank from the jets. Stereoscopic particle image velocimetry (SPIV) is used to make measurements in the midplane of the tank ($z = 0$). This involves two Imager PRO-X cameras (1600×1200 pixels) that are fitted with 105-mm Nikkor lenses mounted on tilt-shift (Scheimpflug) adapters and arranged stereoscopically looking into the tank from the side wall. The viewing angle is 35° to the x axis, and water-filled prisms are installed on the side wall to minimize distortion. The resulting images have a field of view of $8.24 \text{ cm} \times 3.79 \text{ cm}$ in the $x \times y$ directions. The flow is seeded with $10\text{-}\mu\text{m}$ silver-coated hollow glass spheres to act as tracers and illumination is

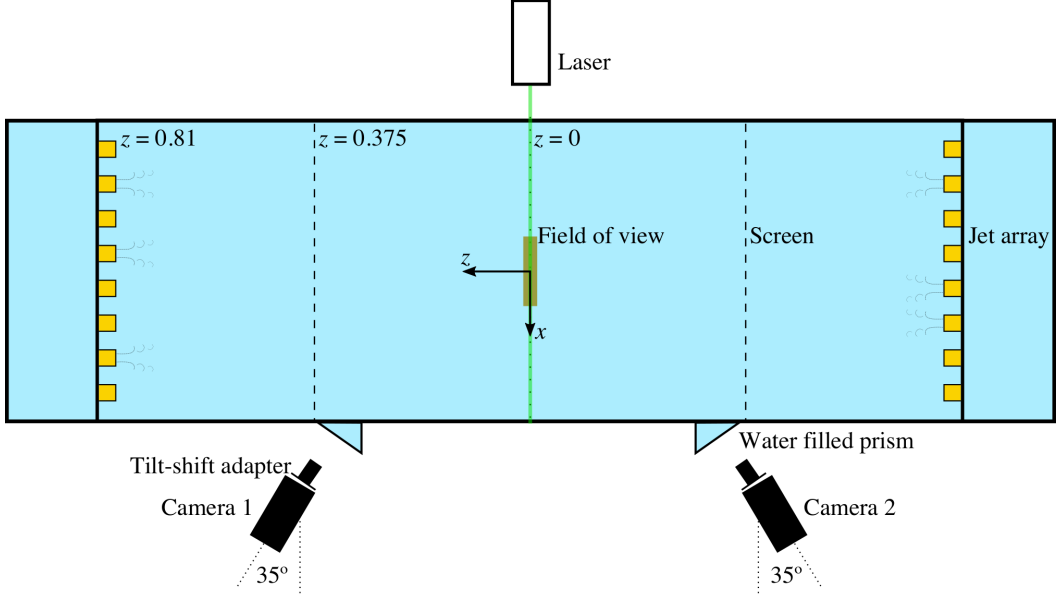


FIG. 1. Top view schematic of the turbulence tank and measurement system. All dimensions are in meters (m).

provided in forward-scatter mode by a frequency-doubled Nd:YAG laser (Big Sky/Quantel). DaVis v7.2 (LaVision) is used to process the images and compute velocity vectors.

The background turbulence is characterized from measurements of the flow without inertial particles present in the tank. For these measurements, velocity field data are collected at 0.5 Hz and the time delay between the successive images of a SPIV image pair is set to 7 ms. Velocity vectors are calculated via a multipass SPIV algorithm where the final pass uses direct correlation with 32×32 pixels subwindows with 50% overlap and a Gaussian weighting function. The turbulence parameters from 560 independent velocity snapshots of the flow are summarized in Table I. The mean dissipation rate, $\langle \epsilon \rangle$, is calculated by the average of the compensated longitudinal second-order velocity structure function over the inertial subrange with a Kolmogorov constant $C_2 = 2.0$. The Taylor length scale is computed by fitting an osculating parabola to the first three points (not including the point at zero lag) of the longitudinal autocorrelation function. Further details on calculation methods and tank performance are provided in Ref. [27].

Inertial particles of three different shapes (cubes, cuboids, and cones) with similar volumes were manufactured for this study using the particle manufacturing process developed in Ref. [29]. The

TABLE I. Parameters of the turbulent flow in the tank.

| Quantity | Value | Units |
|--|-----------------------|----------------------------|
| Turbulence velocity scale, $u_T = [(\langle u_x^2 \rangle + \langle u_y^2 \rangle + \langle u_z^2 \rangle)/3]^{1/2}$ | 2.03×10^{-2} | ms^{-1} |
| Mean dissipation rate, $\langle \epsilon \rangle$ | 5.3×10^{-5} | $\text{m}^2 \text{s}^{-3}$ |
| Taylor length scale, λ_f | 12.6×10^{-3} | m |
| Integral length scale, L | 80.0×10^{-3} | m |
| Kolmogorov length scale, $\eta = (\nu^3/\langle \epsilon \rangle)^{1/4}$ | 0.36×10^{-3} | m |
| Kolmogorov time scale, $\tau_\eta = (\nu/\langle \epsilon \rangle)^{1/2}$ | 0.14 | s |
| Turbulence Reynolds number, $Re_\lambda = u_T \lambda_f / \nu$ | 261 | |

TABLE II. Particle dimensions with 95% confidence intervals computed using Student's t distribution from 30–50 samples. For the cone and the cylinders, the diameter $=d_1 = d_2$ and the height $=d_3$. d_{eq} is the equivalent diameter, i.e., the diameter of a sphere having the same volume as the particle.

| Particle | d_1 (mm) | d_2 (mm) | d_3 (mm) | d_{eq} (mm) |
|-----------------|----------------|----------------|----------------|----------------|
| Cube | 8.2 ± 0.1 | 8.2 ± 0.1 | 8.2 ± 0.1 | 10.1 ± 0.1 |
| Cuboid | 4.0 ± 0.1 | 7.7 ± 0.1 | 15.7 ± 0.4 | 9.8 ± 0.2 |
| Cone | 10.9 ± 0.1 | 10.9 ± 0.1 | 10.0 ± 0.2 | 8.4 ± 0.1 |
| Small cylinder | 4.8 ± 0.1 | 4.8 ± 0.1 | 5.0 ± 0.2 | 4.9 ± 0.1 |
| Medium cylinder | 8.1 ± 0.2 | 8.1 ± 0.2 | 7.8 ± 0.3 | 8.0 ± 0.3 |
| Large cylinder | 19.7 ± 0.5 | 19.7 ± 0.5 | 20.6 ± 1.0 | 20.0 ± 0.5 |
| Long cylinder | 5.1 ± 0.2 | 5.1 ± 0.2 | 19.0 ± 0.8 | 7.9 ± 0.2 |

procedure involves mixing 0.4% agarose polymer by mass and 0.2% commercial glitter by mass with deionized water at 100 °C, which forms a hydrogel upon cooling that is index-of-refraction matched with water and has a density that is a few percent above that of water. To get the desired shapes, the liquid mixture is poured into baking trays to the desired height while accounting for evaporative losses during cooling. Particles are stamped out from the hydrogel sheet using custom-made square and rectangular tubes to make cube-shaped and cuboid-shaped particles, respectively. Cone-shaped particles are manufactured by pouring the mixture into a silicone mold that is custom-made from a 3D-printed positive mould. Table II gives the dimensions of the particles manufactured for this study and the dimensions of the cylinders from Ref. [26].

Separate experiments are performed for each particle shape. In each experiment, particles are added to the tank's central region at a volume fraction of less than 0.5%. Data collection proceeds in loops, where within each loop velocity data is taken at 14 Hz until the onboard camera memory is full (approximately 12 s), at which point the data are transferred to the computer hard drive. For each shape, approximately 1000 such loops are collected and, on average, approximately one particle wanders through the light sheet in the field of view of the cameras per loop. When a particle enters the field of view, laser light passes through the hydrogel and illuminates the glitter. The velocity of the glitter, which acts as a tracer locked in the hydrogel, is measured with the SPIV system. Particles are identified by preprocessing images using an average intensity threshold. Within images, the area occupied by the particle is identified using an edge-preserving median filter combined with a local intensity threshold. Velocity vectors are calculated via a multipass algorithm where the final pass uses direct correlation with 64×64 pixels subwindows with 50% overlap and square top-hat weighting function. Spurious vectors, which constitute less than 5% of the total vectors, are identified and removed in postprocessing by using the normalized median test described in Ref. [30].

B. Computing particle rotation

The particle angular velocity vector, $\boldsymbol{\omega}_p = (\omega_{p_x}, \omega_{p_y}, \omega_{p_z})$, can be calculated from the velocity vectors inside the particle in two ways: (i) using velocity differences in the equation for solid-body rotation as outlined in Bellani *et al.* [23] or (ii) fitting the velocity measurements directly to the equation for solid-body rotation. Both methods operate on finding the linear velocity variation within the particle. As explained in Ref. [23], the velocity-differences method solves the solid-body rotation equation using velocity differences between vector pairs and vector triplets. Since the velocity vectors are measured in the $z = 0$ plane, the ω_{p_z} component can be computed from differences between vector pairs, but the ω_{p_x} and ω_{p_y} components require vector triplets. By cycling through all combinations of vector pairs and triplets, many estimates of the particle angular velocity are produced and the median of this distribution is chosen as the final value. This is very similar to a Theil-Sen estimate (e.g., see Ref. [31]), which is known to compete well with ordinary least squares and be robust to outliers.

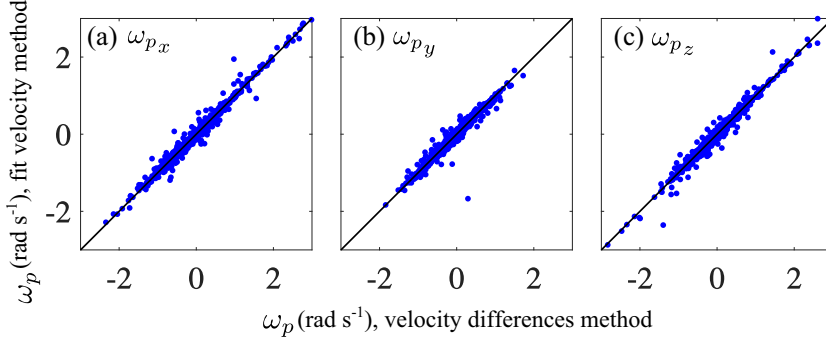


FIG. 2. Particle angular velocity for a subset of cube data calculated from two different methods described in the text. The solid line shows the 1:1 correspondence.

In the fit-velocity method, the linear velocity variation within the particle is fitted directly to the solid-body rotation equation using nonlinear regression. Using the measured velocity vector components ($v_{x_*}, v_{y_*}, v_{z_*}$) at locations (x_*, y_*) in the $z = 0$ plane, the ω_{p_z} component is calculated by fitting the data to the lines given by

$$v_{x_*} = -\omega_{p_z} y_* + C_x, \quad (1a)$$

$$v_{y_*} = \omega_{p_z} x_* + C_y, \quad (1b)$$

where C_x and C_y are fitting parameters that are discarded because the center of volume is not known. The value of ω_{p_z} is taken as the average of the two estimates. The ω_{p_x} and ω_{p_y} components are calculated by fitting the data to the plane given by

$$v_{z_*} = \omega_{p_x} y_* - \omega_{p_y} x_* + C_z, \quad (2)$$

where C_z is again a fitting parameter that is discarded, similar to the C_x and C_y in Eqs. (1).

The velocity-differences method and the fit-velocity method yield very similar results, as shown in Fig. 2, but the advantages of the fit-velocity method are that it is significantly faster to compute and the standard error in each measurement can be obtained directly from the nonlinear regression. This error can be significant since the particle angular velocity is measured via velocity variation over a small distance in which the velocity vectors have noise associated with the SPIV system. Removing the effects of measurement noise in statistics of the particle angular velocity is discussed in the following section.

In both methods described above, it is useful to set the minimum cross-sectional area of a particle for which the angular velocity will be calculated. This is an important threshold in the analysis because a larger cross-sectional area gives a greater number of velocity vectors inside the particle, which reduces the uncertainty in the particle angular velocity and guards against the possibility of stray pieces of hydrogel being mistaken for a particle. We set the threshold to minimum value of 20 vectors for the particles manufactured for this study, which is close to the expected number of vectors when the particles are bisected by the light sheet.

III. RESULTS AND DISCUSSION

A. Particle rotation

The results of particle rotation for the cubes, cuboids, and cones are summarized in Table III. The table also contains results of cylinders, which are from data collected using similar procedures in

TABLE III. The mean and root-mean-square values of particle angular velocity components, and the root-mean-square values of the uncertainties in measurements of particle angular velocity components (rad s^{-1}).

| Particle | $\langle\omega_{p_x}\rangle$ | $\langle\omega_{p_y}\rangle$ | $\langle\omega_{p_z}\rangle$ | $\langle\omega_{p_x}^2\rangle^{1/2}$ | $\langle\omega_{p_y}^2\rangle^{1/2}$ | $\langle\omega_{p_z}^2\rangle^{1/2}$ | $\langle\delta\omega_{p_x}^2\rangle^{1/2}$ | $\langle\delta\omega_{p_y}^2\rangle^{1/2}$ | $\langle\delta\omega_{p_z}^2\rangle^{1/2}$ |
|-----------------|------------------------------|------------------------------|------------------------------|--------------------------------------|--------------------------------------|--------------------------------------|--|--|--|
| Cube | 0.01 | -0.03 | -0.02 | 0.73 | 0.45 | 0.51 | 0.13 | 0.10 | 0.12 |
| Cuboid | 0.00 | 0.00 | -0.01 | 0.68 | 0.54 | 0.62 | 0.14 | 0.12 | 0.14 |
| Cone | 0.01 | 0.03 | -0.03 | 0.72 | 0.53 | 0.67 | 0.13 | 0.12 | 0.14 |
| Small cylinder | 0.01 | 0.07 | -0.05 | 1.18 | 1.04 | 1.02 | 0.20 | 0.19 | 0.54 |
| Medium cylinder | -0.01 | -0.07 | 0.01 | 0.76 | 0.62 | 0.68 | 0.07 | 0.07 | 0.15 |
| Large cylinder | 0.00 | 0.01 | 0.01 | 0.44 | 0.34 | 0.39 | 0.03 | 0.03 | 0.06 |
| Long cylinder | 0.08 | 0.01 | -0.06 | 0.81 | 0.81 | 0.70 | 0.19 | 0.17 | 0.41 |

the same facility and were originally presented in Ref. [26]. The vector fields from that dataset have been reanalyzed using the fit-velocity method to allow consistent comparison.

Since the background flow is isotropic, the components of particle angular velocity have means that are close to zero and much smaller than the root-mean-square (rms) values (see Table III). We observe that the rms value of ω_{p_x} is generally greater than that of the other components; this is due to the fact that the particles are slightly negatively buoyant [29] and hence spend a greater amount of time near the bottom of the tank where the flow is anisotropic and the component of fluid vorticity in the $\pm x$ directions is higher than the other components.

We are interested in the mean square of the total particle angular velocity, $\langle\omega_p^2\rangle = \langle\omega_{p_x}^2\rangle + \langle\omega_{p_y}^2\rangle + \langle\omega_{p_z}^2\rangle$, but its value calculated from the data is expected to be larger than its actual value due to measurement noise. Each measurement of a particle angular velocity component can be thought of as the sum of its actual value and the measurement uncertainty: $\omega_{p_x} = \omega_{p_{x,a}} \pm \delta\omega_{p_x}$. The mean-square value of that component is then given by $\langle\omega_{p_x}^2\rangle = \langle(\omega_{p_{x,a}} \pm \delta\omega_{p_x})^2\rangle = \langle\omega_{p_{x,a}}^2\rangle + \langle\delta\omega_{p_x}^2\rangle \pm 2\langle\omega_{p_{x,a}}\delta\omega_{p_x}\rangle$. The pure noise term is known since we have $\delta\omega_{p_i}$ in each measurement from the nonlinear regression. Assuming that the uncertainty in a measurement is not correlated with the actual value and that the distribution of the actual values has zero mean, the final term in the mean-square expansion vanishes, i.e., $2\langle\omega_{p_{x,a}}\delta\omega_{p_x}\rangle = 2\langle\omega_{p_{x,a}}\rangle\langle\delta\omega_{p_x}\rangle = 0$. Thus, the contribution of the measurement noise to the mean-square value can be removed by subtracting off the mean-square uncertainties from each component: $\langle\omega_{p_{x,a}}^2\rangle = \langle\omega_{p_x}^2\rangle - \langle\delta\omega_{p_x}^2\rangle$. We use this procedure to remove the effects of measurement noise from the total mean-square particle angular velocity in Fig. 3.

In Fig. 3, we plot the total mean-square particle angular velocity as a function of particle size, where size is characterized by the equivalent diameter of a volume-matched sphere, d_{eq} . These quantities are made dimensionless by the Kolmogorov scales, τ_η and η , respectively. The data appear to follow a scaling law shown by the dashed lines: For all particle types, regardless of shape, the mean-square particle angular velocity falls off as $d_{eq}^{-4/3}$. This scaling is consistent with the original Kolmogorov similarity hypotheses (K41 theory). If we postulate that turbulent motions of size d_{eq} , with a turnover timescale $\tau_{d_{eq}}$, are the primary source of particle rotations, then the mean-square particle angular velocity should scale as $\langle\omega_{p_a}^2\rangle \sim \tau_{eq}^{-2}$. For d_{eq} in the inertial subrange, K41 theory relates τ_{eq} to d_{eq} and the mean dissipation rate via the scaling relation $\tau_{d_{eq}} \sim d_{eq}/(d_{eq}\epsilon)^{1/3}$. Substituting this into the scaling relation of the mean-square particle angular velocity gives $\langle\omega_{p_a}^2\rangle \sim d_{eq}^{-4/3}$. This type of scaling was introduced by Parsa and Voth [11] for tumbling of thin fibers in turbulence and by Bordoloi and Variano [26] for rotations of inertial cylinders with aspect ratios 1:1 and 1:4. Here, we find that cubes and cones with aspect ratio 1:1 and cuboids with aspect ratio 1:2:4 also agree with this scaling. This provides evidence for the fact that d_{eq} is the relevant measure of particle size for characterizing rotations of the inertial particles of the type we have tested in turbulence.

In Fig. 4, we consider the particle angular velocity distributions by plotting probability density functions (PDFs) of measured particle angular velocity components normalized by their respective

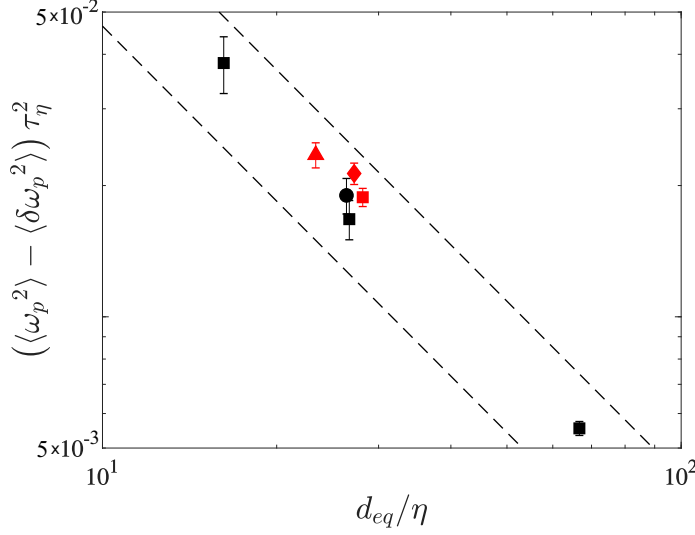


FIG. 3. Dimensionless mean-square particle angular velocity plotted against the dimensionless particle size measured by the diameter of a volume-matched sphere. The mean-square uncertainty, $\langle \delta \omega_p^2 \rangle = \langle \delta \omega_{p_x}^2 \rangle + \langle \delta \omega_{p_y}^2 \rangle + \langle \delta \omega_{p_z}^2 \rangle$, is subtracted from the mean-square particle angular velocity, $\langle \omega_p^2 \rangle = \langle \omega_{p_x}^2 \rangle + \langle \omega_{p_y}^2 \rangle + \langle \omega_{p_z}^2 \rangle$, to remove the effects of measurement noise as explained in the text. Data of cubes (red square), cuboids (red diamond), and cones (red triangle) are plotted along with small, medium, and large cylinders (black squares) and long cylinders (black circle). Cylinder data (black symbols) have been made dimensionless by $\eta = 0.3 \times 10^{-3}$ m and $\tau_\eta = 0.11$ s, as reported in Ref. [26]. The 95% confidence interval uncertainty bars are calculated from a bootstrap analysis. The dashed lines are given by $(d_{eq}/\eta)^{-4/3}$ and $2(d_{eq}/\eta)^{-4/3}$.

rms values. They show good fits to the model given by

$$P(a) = \frac{\exp(3s^2/2)}{4\sqrt{3}} \left[1 - \operatorname{erf} \left(\frac{\ln|a/\sqrt{3}| + 2s^2}{s\sqrt{2}} \right) \right]. \quad (3)$$

This model is derived by assuming that the magnitude of the angular velocity vector follows a log-normal distribution and the direction of the angular velocity vector is isotropic with respect to the laboratory frame. Zimmermann *et al.* [19] and Klein *et al.* [18] have previously shown that this model provides good fits to data of angular velocity components of inertial spheres in turbulence. The values of the dimensionless fitting parameter, s , are listed in Table IV.

We have studied the effect of measurement noise on the value of s via simulations of the data collection and analysis, similar to Ref. [24]. We generate noise-free particle angular velocity vectors that are isotropically distributed with vector magnitudes that are log-normally distributed with variance that match data of cubes, cuboids, and cones. Next, the angular velocity vectors are converted to synthetic velocity measurements arranged in a rectangular array in the $z = 0$ plane. The number of synthetic velocity vectors to be created is decided by drawing from a uniform distribution spanning the interval 20–50, which is similar to the data for cubes, cuboids, and cones. Gaussian random noise is added to the velocity vectors with variance that matches the known noise level in the SPIV data. The noisy velocity vectors are then processed using the fit-velocity method described above to arrive at synthetic measurements of particle angular velocities. The synthetic data show that noise in the velocity vectors increases the mean-square particle angular velocity and can be corrected for as described above. More importantly, the synthetic data show that noise in the velocity vectors only slightly reduces the value of s , by an amount on the order of the uncertainty bounds in fitting Eq. (3)

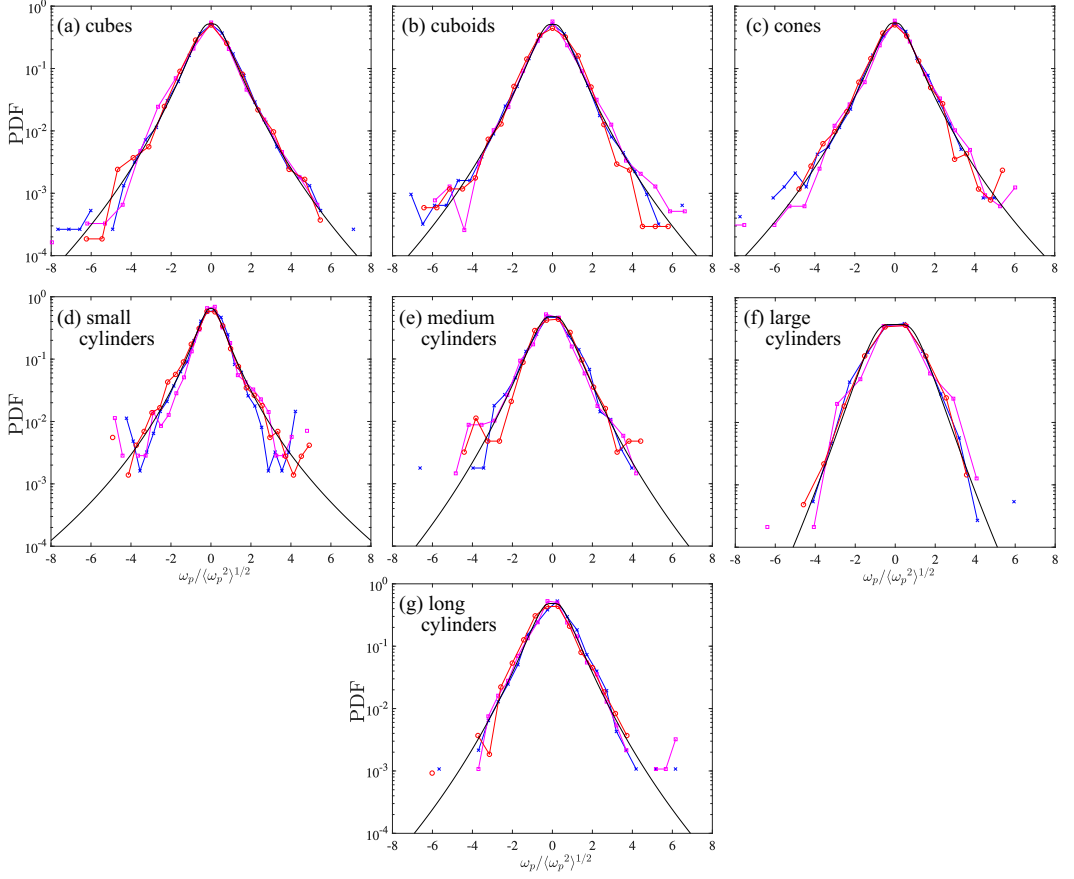


FIG. 4. Probability density functions (PDFs) of particle angular velocity components normalized by their rms values: blue crosses, ω_{p_x} ; magenta squares, ω_{p_y} ; red circles, ω_{p_z} . (a) Cubes, (b) cuboids, (c) cones, (d) small cylinders, (e) medium cylinders, (f) large cylinders, and (g) long cylinders. The PDFs are fitted to Eq. (3) and the fitting parameter, s , is listed in Table IV.

to the data. We conclude from this that the shape of the PDFs are not overly affected by measurement noise.

From Table IV and Fig. 5, we observe that the PDFs are super-Gaussian with heavy tails for all particles and that the value of s is a function only of particle size as measured by d_{eq} . Cubes, cuboids,

TABLE IV. The fitting parameter, s , for the PDFs of the particle angular velocity components in Eq. (3) and its 95% confidence intervals from the fit. K is the kurtosis of the PDF calculated using Eq. (3) for each value of s .

| Particle | s | K |
|-----------------|-----------------|----------------|
| Cube | 0.63 ± 0.01 | 8.6 ± 0.4 |
| Cuboid | 0.62 ± 0.01 | 8.2 ± 0.4 |
| Cone | 0.64 ± 0.01 | 9.4 ± 0.5 |
| Small cylinder | 0.73 ± 0.02 | 14.8 ± 1.5 |
| Medium cylinder | 0.58 ± 0.02 | 6.9 ± 0.6 |
| Large cylinder | 0.41 ± 0.01 | 3.5 ± 0.1 |
| Long cylinder | 0.59 ± 0.02 | 7.1 ± 0.7 |

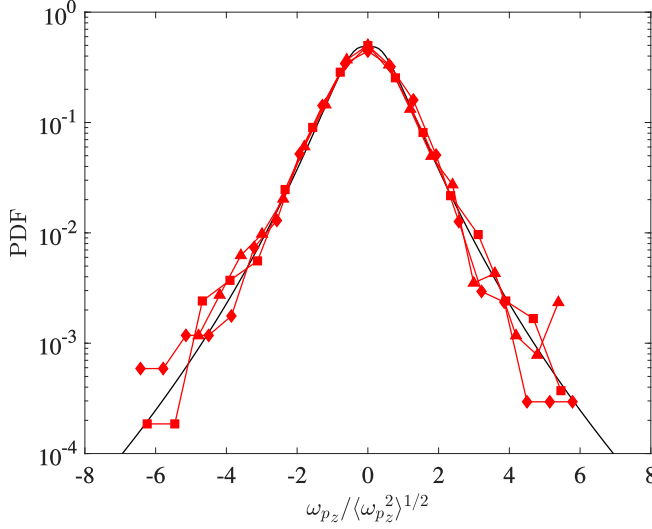


FIG. 5. Probability density functions (PDFs) of one component of particle angular velocity normalized by its rms value. Data of cubes (red squares), cuboids (red diamonds), and cones (red triangles) are plotted along with Eq. (3) with $s = 0.63$, which is the average value across the three shapes (see Table IV).

and cones have PDFs with very similar shapes despite the difference in particle shapes. We also observe that s increases as d_{eq} decreases. In other words, the tails of the PDF become heavier for smaller particles.

The model PDF in Eq. (3) with the fitting parameter s can be used to calculate the kurtosis of the particle angular velocity components, which can then be compared to the kurtosis of velocity increments in the flow, i.e., velocity structure functions. This comparison should give insight into whether turbulent motions of size d_{eq} also control the extreme events in rotations of inertial particles. The kurtosis of the particle angular velocity components is calculated via numerically evaluating the integral $\int_{-\infty}^{\infty} a^4 P(a) da$ for $P(a)$ given by Eq. (3). The kurtosis values are listed in Table IV. For comparison to particle angular velocity, we choose to calculate the kurtosis of the transverse velocity increments in the flow $\langle \Delta_x u_y^4 \rangle / \langle \Delta_x u_y^2 \rangle^2$, where $\Delta_x u_y$ is the velocity increment in u_y across a given separation distance in the x direction. The kurtosis values of velocity increments over distances in the inertial subrange in turbulence are known to increase with decreasing scale due to internal intermittency [32]. Thus, we also compare these kurtosis values with the predictions of the refined Kolmogorov hypotheses (K62 theory). In this theory, the moments of velocity increments are conditioned on the moments of the locally averaged value of the dissipation rate, which itself is assumed to follow a log-normal distribution (e.g., see Ref. [33]). The moments of velocity increments in the inertial subrange are predicted to scale with the separation distance, d_{eq} , as $\langle [\Delta_x u_y]^n \rangle \sim d_{eq}^{(n/3) - \mu(n/6)[(n/3) - 1]}$. Taking the value of the intermittency exponent as $\mu = 0.25$ gives the scaling prediction for kurtosis of velocity increments to be $\sim d_{eq}^{-0.11}$.

The kurtosis values of particle angular velocity components and those of the transverse velocity increments in the flow are shown in Fig. 6 together with the predicted scaling law from K62 theory. The predicted scaling law (dashed line) seems to describe the data of $\langle \Delta_x u_y^4 \rangle / \langle \Delta_x u_y^2 \rangle^2$ (solid line) for $d_{eq}/\eta > 60$. However, the kurtosis values for the particle angular velocity components do not follow the kurtosis values of velocity increments in the flow or the prediction of K62 theory. We make three further observations from the data in Fig. 6: (i) for all particles, the kurtosis is larger than the value of a Gaussian distribution ($K = 3$); (ii) for $d_{eq}/\eta < 30$, particle angular velocity components appear to have a higher kurtosis than transverse velocity increments; and (iii) the kurtosis of particle angular velocity components seems to fall off at a much steeper rate (close to d_{eq}^{-1}) than that of

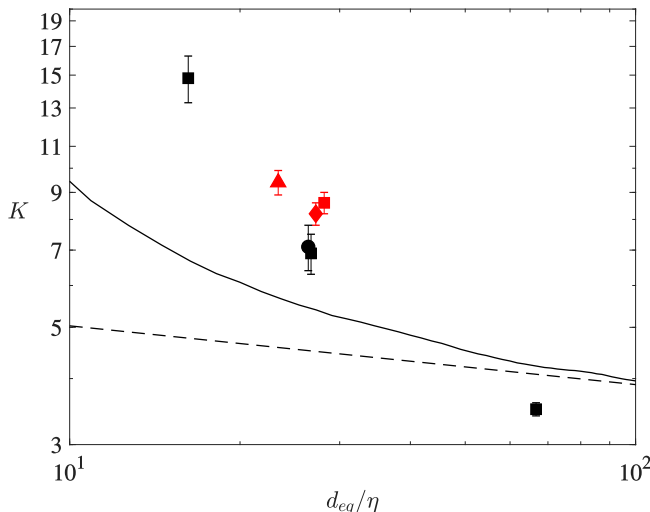


FIG. 6. Kurtosis values of particle angular velocity components and transverse velocity increments in the flow. A Gaussian distribution would have a value of $K = 3$. The symbols are the same as Fig. 3 and their error bars are calculated from the 95% confidence intervals on the fitting parameter, s , and listed in Table IV. Cylinder data (black symbols) have been made dimensionless by $\eta = 0.3 \times 10^{-3}$ m, as reported in Ref. [26]. The solid line is $\langle \Delta_x u_y^4 \rangle / \langle \Delta_x u_y^2 \rangle^2$ and the dashed line shows the power law $d_{eq}^{-0.11}$.

transverse velocity increments. We interpret these results as the effects of particle inertia, which is further discussed in the following section.

B. Discussion

The results of this study point to the fact that the majority of the particle rotations in turbulence are primarily due to turbulent motions of size d_{eq} or larger. This is supported by the collapse of the mean-square particle angular velocity onto a common power law based on d_{eq} . It is also supported by the collapse of standardized PDFs for particle angular velocity components of particles with different shapes and similar d_{eq} . It seems that particle shape plays a very minor role, if any at all, in determining rotation of the inertial particles that have low aspect ratios and dimensions that exceed the Kolmogorov scale in all three particle axes.

It is instructive to compare the rotations of inertial particles tested here to those of four thin rods arranged in a tetrahedral “skeleton” developed by Voth and collaborators [34]. These shapes have length scales in the inertial subrange, but much less particle inertia than the particles tested here. Data from Ref. [34] on the rotation of such particles show that $\langle \omega_p^2 \rangle \tau_\eta^2 \approx 8(d/\eta)^{-4/3}$, where d is the diameter of the sphere that circumscribes the tetrad and falls in the inertial subrange. The coefficient of 8 is precisely the result that would be expected if transverse velocity increments at a scale of d were rotating the tetrads. This can be seen from the K41 theory of transverse velocity increments: Denote $\langle \Delta_N u^2 \rangle$ as the mean-square of transverse velocity increments in the flow at scale d and then postulate that without particle inertia, the mean-square particle angular velocity will be given by $\langle \omega_p^2 \rangle = 3\langle \Delta_N u^2 \rangle / d^2$. The factor of 3 is required to include all three components of particle rotation (in the laboratory frame). Substituting in the prediction of K41 theory $\langle \Delta_N u^2 \rangle = (4/3)C_2(\epsilon d)^{2/3}$ with $C_2 = 2.0$ gives $\langle \omega_p^2 \rangle \tau_\eta^2 = 8.0(d/\eta)^{-4/3}$.

We can discern the effect of inertia by comparing the power-law coefficient of 8.0 in Ref. [34] to the coefficient for our data, which is between 1 and 2. It seems particle inertia reduces the mean-square particle angular velocity by a factor in the interval 4–8. Our data show that this decrease occurs

without disturbing the power law scaling in the inertial subrange, which is predicted by K41 theory and observed in the second-order fluid velocity statistics.

Interestingly, the fourth-order fluid velocity statistics show a power law that is not at all matched by the data of inertial particle rotation. This implies that extreme events of particle rotation do not occur with the same frequency as extreme events in fluid motions of size d_{eq} . The kurtosis values of particle angular velocity components for $d_{eq}/\eta < 30$ seem to suggest that the PDFs of particle angular velocity have heavier tails than that of velocity increments at the same scale. Our interpretation of these data are that only the very rare and energetic turbulent motions cause particle rotations that are large multiples of the rms value, but they are likely to be sustained for longer than the turbulent motions when they do occur. Comparing the trend in our kurtosis values to those of angular velocities of inertial spheres reported in Ref. [18] ($K = 6$ for $d/\eta = 100$) and Ref. [19] ($K = 4$ for $d/\eta = 600$), we note that there does not seem to be a consistent power law behavior from all the data. Thus, more data of extreme events of particle rotations is required to establish a firm scaling law (if it exists). While the precise kurtosis values reported here should be interpreted with caution since that they are computed via fits to the measured PDF, the data do seem to show a clear trend of decreasing kurtosis with increasing particle size.

IV. CONCLUSIONS

The main conclusion from this study is that the appropriate scale to characterize rotations of low-aspect-ratio inertial particles of different shapes in turbulence is d_{eq} , the equivalent diameter of a volume-matched sphere. The mean-square rotation rate of the inertial particles we tested scale as $d_{eq}^{-4/3}$, which is consistent with the predictions of K41 theory assuming that transverse velocity increments in the flow can be directly related to particle rotation. The physical picture that emerges from this scaling relationship is that particles stop responding to the energy cascade at a scale of d_{eq} , despite a factor of 2 difference between d_{eq} and the shortest or longest particle dimension. Further evidence of the importance of d_{eq} is provided by the standardized PDFs, which collapse for different particle shapes at a given d_{eq} . Thus, the statistics of particle rotation measured in the laboratory frame have been found to be insensitive to particle shape. However, certain applications, e.g., modeling plankton, require knowledge of particle rotations about specific particle axes, which may still be influenced by particle shape. We envisage that future investigations that measure particle rotation in the particle frame will be able to make further inroads into this problem.

ACKNOWLEDGMENTS

The authors acknowledge funding from the US Army Research Office (Grant No. W911NF-16-1-0284) and the National Science Foundation (Grant No. CBET-1604026). The authors would also like to thank Palak Thakur for help with laboratory experiments and Gautier Verhille, Greg Voth, Margaret Byron, and Colin Meyer for fruitful conversations.

-
- [1] F. Toschi and E. Bodenschatz, Lagrangian properties of particles in turbulence, [Annu. Rev. Fluid Mech.](#) **41**, 375 (2009).
 - [2] S. Balachandar and J. K. Eaton, Turbulent dispersed multiphase flow, [Annu. Rev. Fluid Mech.](#) **42**, 111 (2010).
 - [3] M. Maxey, Simulation methods for particulate flows and concentrated suspensions, [Annu. Rev. Fluid Mech.](#) **49**, 171 (2017).
 - [4] M. Bourgoin and H. Xu, Focus on dynamics of particles in turbulence, [New J. Phys.](#) **16**, 085010 (2017).
 - [5] M. R. Maxey and J. J. Riley, Equation of motion for a small rigid sphere in a nonuniform flow, [Phys. Fluids](#) **26**, 883 (1983).

- [6] E. Loth and A. J. Dorgan, An equation of motion for particles of finite Reynolds number and size, *Environ. Fluid Mech.* **9**, 187 (2009).
- [7] E. Calzavarini, R. Volk, M. Bourgoïn, E. L  v  que, J. F. Pinton, and F. Toschi, Acceleration statistics of finite-sized particles in turbulent flow: The role of Fax  n forces, *J. Fluid Mech.* **630**, 179 (2009).
- [8] H. Homann and J. Bec, Finite-size effects in the dynamics of neutrally buoyant particles in turbulent flow, *J. Fluid Mech.* **651**, 81 (2010).
- [9] H. Xu and E. Bodenschatz, Motion of inertial particles with size larger than Kolmogorov scale in turbulent flows, *Phys. D (Amsterdam, Neth.)* **237**, 2095 (2008).
- [10] M. Shin and D. L. Koch, Rotational and translational dispersion of fibres in isotropic turbulent flows, *J. Fluid Mech.* **540**, 143 (2005).
- [11] S. Parsa and G. A. Voth, Inertial Range Scaling in Rotations of Long Rods in Turbulence, *Phys. Rev. Lett.* **112**, 024501 (2014).
- [12] S. Parsa, E. Calzavarini, F. Toschi, and G. A. Voth, Rotation Rate of Rods in Turbulent Fluid Flow, *Phys. Rev. Lett.* **109**, 134501 (2012).
- [13] L. Chevillard and C. Meneveau, Orientation dynamics of small, triaxial-ellipsoidal particles in isotropic turbulence, *J. Fluid Mech.* **737**, 571 (2013).
- [14] R. Ni, N. T. Ouellette, and G. A. Voth, Alignment of vorticity and rods with Lagrangian fluid stretching in turbulence, *J. Fluid Mech.* **743**, R3 (2014).
- [15] G. A. Voth and A. Soldati, Anisotropic particles in turbulence, *Annu. Rev. Fluid Mech.* **49**, 249 (2017).
- [16] G. B. Jeffery, The motion of ellipsoidal particles immersed in a viscous fluid, *Proc. R. Soc. London, Ser. A* **102**, 161 (1922).
- [17] N. Pujara and E. Variano, Rotations of small, inertialess triaxial ellipsoids in isotropic turbulence, *J. Fluid Mech.* **821**, 517 (2017).
- [18] S. Klein, M. Gibert, A. B  rut, and E. Bodenschatz, Simultaneous 3D measurement of the translation and rotation of finite-size particles and the flow field in a fully developed turbulent water flow, *Meas. Sci. Technol.* **24**, 024006 (2012).
- [19] R. Zimmermann, Y. Gasteuil, M. Bourgoïn, R. Volk, A. Pumir, and J.-F. Pinton, Tracking the dynamics of translation and absolute orientation of a sphere in a turbulent flow, *Rev. Sci. Instrum.* **82**, 033906 (2011).
- [20] L. Fiabane, R. Zimmermann, R. Volk, J. F. Pinton, and M. Bourgoïn, Clustering of finite-size particles in turbulence, *Phys. Rev. E* **86**, 035301 (2012).
- [21] R. Zimmermann, Y. Gasteuil, M. Bourgoïn, R. Volk, A. Pumir, and J.-F. Pinton, Rotational Intermittency and Turbulence Induced Lift Experienced by Large Particles in a Turbulent Flow, *Phys. Rev. Lett.* **106**, 154501 (2011).
- [22] A. Naso and A. Prosperetti, The interaction between a solid particle and a turbulent flow, *New J. Phys.* **12**, 033040 (2010).
- [23] G. Bellani, M. L. Byron, A. G. Collignon, C. R. Meyer, and E. A. Variano, Shape effects on turbulent modulation by large nearly neutrally buoyant particles, *J. Fluid Mech.* **712**, 41 (2012).
- [24] C. R. Meyer, M. L. Byron, and E. A. Variano, Rotational diffusion of particles in turbulence, *Limnol. Oceanogr.* **3**, 89 (2013).
- [25] M. Byron, J. Einarsson, K. Gustavsson, G. Voth, B. Mehlig, and E. Variano, Shape dependence of particle rotation in isotropic turbulence, *Phys. Fluids* **27**, 035101 (2015).
- [26] A. D. Bordoloi and E. Variano, Rotational kinematics of large cylindrical particles in turbulence, *J. Fluid Mech.* **815**, 199 (2017).
- [27] G. Bellani and E. A. Variano, Homogeneity and isotropy in a laboratory turbulent flow, *Exp. Fluids* **55**, 1646 (2014).
- [28] E. A. Variano and E. A. Cowen, A random-jet-stirred turbulence tank, *J. Fluid Mech.* **604**, 1 (2008).
- [29] M. L. Byron and E. A. Variano, Refractive-index-matched hydrogel materials for measuring flow-structure interactions, *Exp. Fluids* **54**, 1456 (2013).
- [30] J. Westerweel and F. Scarano, Universal outlier detection for PIV data, *Exp. Fluids* **39**, 1096 (2005).
- [31] M. Hollander, D. A. Wolfe, and E. Chicken, *Nonparametric Statistical Methods* (John Wiley & Sons, New York, 2013).

- [32] U. Frisch, *Turbulence: The Legacy of A. N. Kolmogorov* (Cambridge University Press, Cambridge, UK, 1995).
- [33] S. B. Pope, *Turbulent Flows* (Cambridge University Press, Cambridge, UK, 2000).
- [34] B. C. Cole, Size dependence of rotation rates of spheres and disks in turbulence, Master's thesis, Wesleyan University, Middletown, Connecticut, 2016 (unpublished).